Experimental Signature of Quantum Turbulence in Velocity Spectra?

Julien Salort, Francesca Chillà, Éléonore Rusaouën, Philippe-E. Roche,
Mathieu Gibert, Iouri Moukharski, Alan Braslau, François Daviaud, Basile
Gallet, Ewe-Wei Saw, et al.

New Journal of Physics

The open access journal at the forefront of physics

PAPER

Experimental signature of quantum turbulence in velocity spectra?

J Salort[1,*] , F Chillà[1] , E Rusaouën[2] , P-E Roche[2] , M Gibert[2], I Moukharski[3],
A Braslau[3], F Daviaud[3], B Gallet[3], E-W Saw[3], B Dubrulle[3] , P Diribarne[4], B Rousset[4],
M Bon Mardion[4], J-P Moro[4], A Girard[4], C Baudet[5], V L'vov[6], A Golov[7] and
S Nazarenko[8]

1   Univ Lyon, ENS de Lyon, Univ Claude Bernard, CNRS, Laboratoire de Physique, Lyon, France
2   Univ. Grenoble Alpes, Institut NEEL, F-38042 Grenoble, France
3   Laboratoire SPHYNX, CEA/IRAMIS/SPEC, CNRS URA 2464, F-91191 Gif-sur-Yvette, France
4   Univ. Grenoble Alpes, IRIG-DSBT, F-38000 Grenoble, France
5   CNRS, LEGI, F-38041 Grenoble, France
6   Department of Chemical and Biological Physics, Weizmann Institute of Science, 7610001 Rehovot, Israel
7   Department of Physics and Astronomy, The University of Manchester, Manchester MP13 9PL, United Kingdom
8   Institut de Physique de Nice, Université Nice-Sophia Antipolis, Parc Valrose, 06108 Nice, France
*   Author to whom any correspondence should be addressed.

E-mail: julien.salort@ens-lyon.fr

Abstract

Velocity measurements in turbulent superfluid helium between *co-rotating* propellers are reported. The parameters are chosen such that the flow is fully turbulent, and its dissipative scales are partly resolved by the velocity sensors. This allows for the first experimental comparison of spectra in quantum *versus* classical turbulence where dissipative scales are resolved. In some specific conditions, differences are observed, with an excess of energy at small scales in the quantum case compared to the classical one. This difference is consistent with the prediction of a pileup of superfluid kinetic energy at the bottom of the inertial cascade of turbulence due to a specific dissipation mechanism.

1. Introduction

Above $T_\lambda \approx 2.18$ K, liquid helium-4 is a classical 'Navier–Stokes' fluid called He I. It is a viscous fluid with the lowest viscosity of all known fluids, $\nu \simeq 2 \times 10^{-8}$ m^2 s^{-1} at 2.3 K and 10^5 Pa. The motivation to use He I in hydrodynamic experiments is the ability to reach very high Reynolds numbers,

$$\mathrm{Re} = LU/\nu, \tag{1}$$

where L is the typical length scale and U the typical velocity of the flow. Indeed, the low value of the viscosity allows for larger Reynolds numbers in laboratory conditions than the counterpart room temperature experiments.

Below T_λ, liquid helium 4 is a non-classical fluid called He II. It behaves as a mixture of two fluids [1], a non-viscous component ('superfluid component'), and a viscous component ('normal component'). The dynamics of turbulent He II is greatly influenced by singularities in the superfluid component called quantum vortices, which form a complex tangle at high Reynolds number. See e.g. reference [2] for a detailed introduction on quantum turbulence. One important question is the dissipation mechanisms in this system, in particular in the zero temperature limit where the density of the normal component vanishes. The turbulence of He II is sometimes called *quantum turbulence*, or *superfluid turbulence*.

Experimental investigation of superfluid turbulence can be split into three categories: (i) investigation with sensors which have classical analogues, (ii) investigation with sensors which do not have a classical analogue, (iii) flow visualization with various kinds of tracers.

In the category (i), all turbulence quantities with a classical analogue were found to be identical in classical and quantum turbulence experiments when conducted at sufficiently high Reynolds number. This category includes drag force [3–6], pressure drop [7, 8], mean-torque [9], statistics of intense vorticity coherent structures [10] and velocity statistics including histograms [11], spectra [12, 13], energy cascade from large to small scales [11] and intermittency [12, 14]. Due to resolution limitation, all studies in this category have unveiled superfluid turbulence properties at the large and intermediate 'inertial' scales of the turbulence cascade, but not within the dissipative range of scales. In other words, the smaller scales of the flow, where quantum effect inevitably prevail due to quantization of the circulation of the superfluid velocity have not yet been resolved. In the category (ii), a quantum quantity has been characterized in fully developed turbulence: the density of superfluid vortex lines [15–21]. Again, only statistics down to the inertial scales of turbulence could be resolved [20, 21]. The optical technics of category (iii) have mostly been implemented at low Reynolds number (i.e. low intensity turbulence) in order to resolve the smallest flow scales [22–32] [9]. In particular, velocity statistics at quantum scales have been reported including histograms and intermittency (eg see [27, 32, 38]).

From a classical turbulence standpoint, the reason for a lack of change above and below the superfluid transition is that the dynamics of turbulent flows at high Reynolds number is fully determined by the large scales [39]. In principle however, this is expected to hold only at scales much larger than the typical inter-vortex distance, where He II behaves as a single fluid. At scales where the two-fluids are decoupled, the statistics should deviate from the classical ones. The inter-vortex distance length scale scales similarly to the classical dissipative range [40]. Due to the low viscosity, the Reynolds number is usually large in helium flows, and the classical dissipative range lies outside sensor resolution. See reference [41] for a review on velocity spectra in particular.

In this work, we report and compare velocity spectra in He I and He II in a large vessel at low velocities. We chose the experimental parameters such that the Reynolds number is large enough for the flow to be fully turbulent, and small enough for the dissipative length scales to lie within the sensor spatial resolution. We find the first experimental evidence of a possible signature of quantum turbulence with a local velocity sensor.

The paper is organized as follows: in the first section, the flow properties are determined in He I using a reference hot-wire anemometer; in the second section a cantilever anemometer and a miniature Pitot-like sensor, which works similarly in both He I and He II are validated against the hot-wire; in the third section, velocity spectra obtained in He II with the cantilever anemometer and the miniature Pitot sensor are discussed.
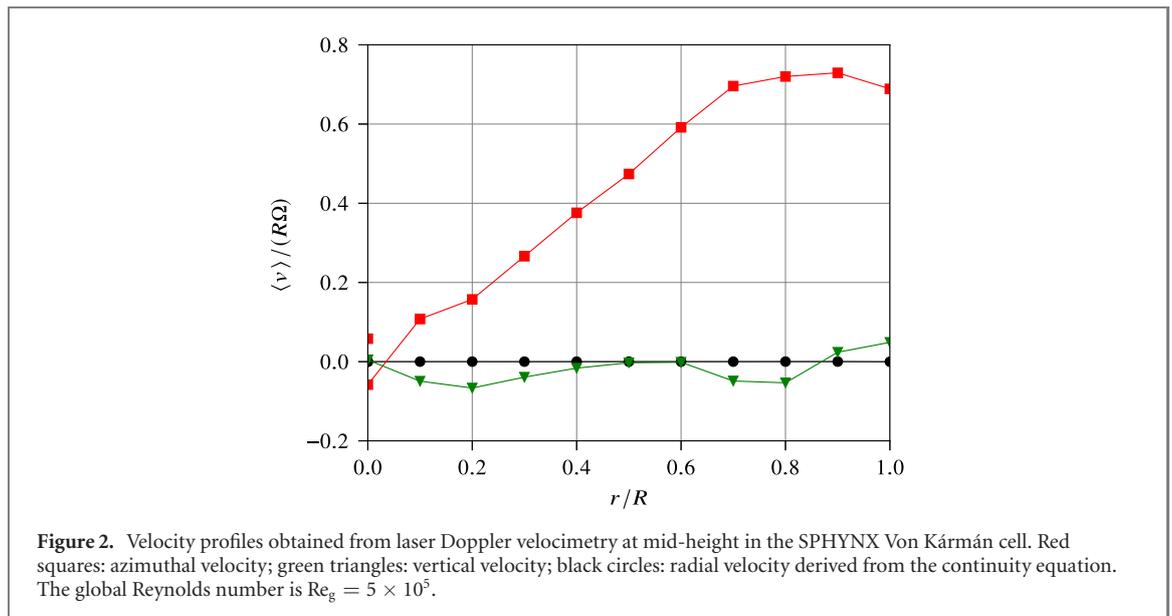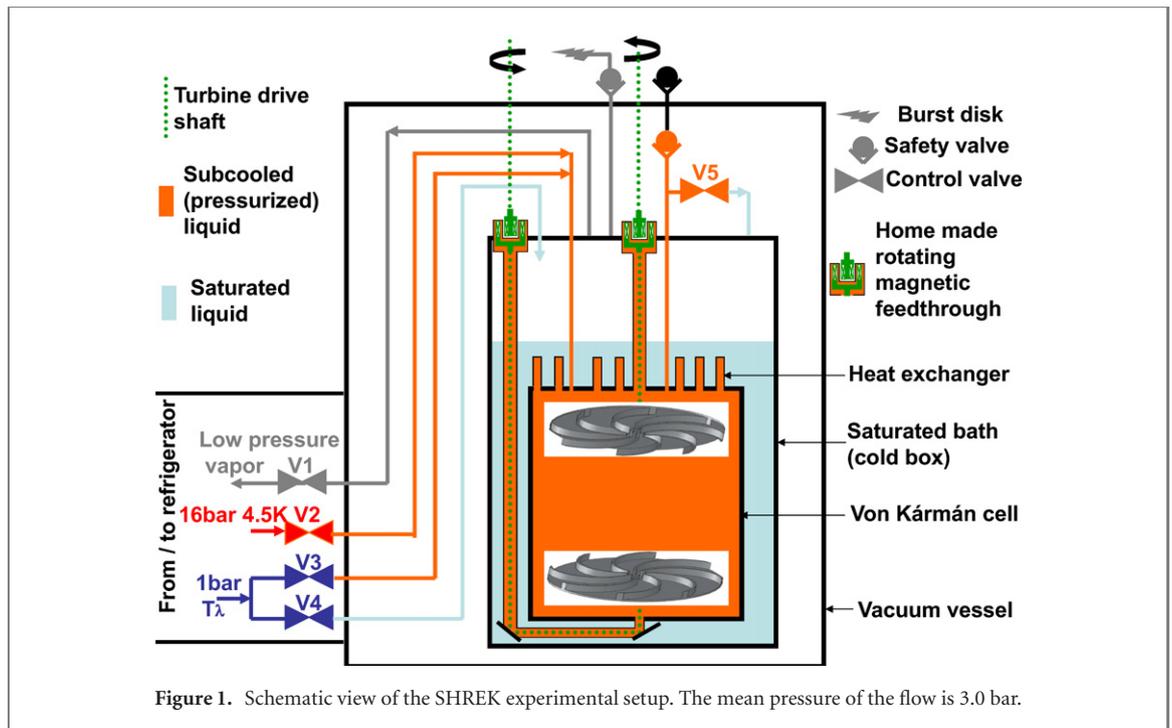
2. Flow characteristics in He I

2.1. Experimental set-up

The SHREK facility is described in details in [42] (see figure 1). We recall here its main characteristics, and the operating conditions, above and below the superfluid transition of helium 4. The flow is enclosed in a cylinder with inner diameter $\Phi = 780$ mm. The fluid is set into motion by two disks fitted with curved blades, located 702 mm apart at the top and the bottom of the cylinder. The curvature of the blades is chosen such that the forcing is symmetric when the disks rotate in opposite angular velocity ('contra-rotation'). For the 'co-rotation' configurations used in this manuscript, the curvature of the blades breaks the symmetry with respect to the mid-plane, possibly inducing higher turbulence intensity than symmetric forcing. The radius of the disks is $R = 360.75$ mm. The height of the blades is 78 mm. The angular velocities of the top propeller, Ω_t, and of the bottom propeller, Ω_b, can be set independently. In this work however, they both rotate at nearly the same angular speed, producing one large vortex inside the tank. We thus denote as $\Omega \simeq \Omega_b \simeq \Omega_t$ the angular velocity, which ranges from 0 to 3.8 rad s^{-1} (the rotation frequency $f = \Omega/(2\pi)$, ranging from 0 to 600 mHz).

A smaller experiment filled with water at room temperature has been operated at SPHYNX laboratory to get insights on the mean flow structure. Laser Doppler Velocimetry (LDV) measurements have been carried out. The geometry is a downscaled version of the SHREK cell, with an inner diameter of 20 cm, and the global Reynolds number is 5×10^5, ranging from 2 to 50 times smaller than the global Reynolds number in the SHREK cell (see below). As can be seen in figure 2, in the exact *co-rotation* regime that we consider, the azimuthal velocity at mid-height, v_θ, is given by solid-body rotation,

$$v_\theta = r\Omega, \tag{2}$$

---

[9] For non-optical investigation of low Reynolds superfluid turbulence, see for instance [33–37].

Figure 1. Schematic view of the SHREK experimental setup. The mean pressure of the flow is 3.0 bar.

Figure 2. Velocity profiles obtained from laser Doppler velocimetry at mid-height in the SPHYNX Von Kármán cell. Red squares: azimuthal velocity; green triangles: vertical velocity; black circles: radial velocity derived from the continuity equation. The global Reynolds number is $Re_g = 5 \times 10^5$.

except close to the walls ($r/R > 0.8$), where the azimuthal velocity gets to a plateau of order $0.75R\Omega$. There has to be a viscous sub-layer and vanishing velocity very close to the wall, but it is too small to be resolved by the LDV measurements. It should get thinner with increasing Reynolds number, therefore vanishingly small in the SHREK apparatus.

The local velocity sensors in the SHREK apparatus are located at mid-height in the equatorial plane, and are described in more details in the following sections: a hot-wire and a miniature Pitot sensor are located 4 cm from the wall, and a cantilever anemometer 1 cm from the wall. Although these sensors are not close to each other, and not exactly at the same distance from the wall, we expect the average properties of the local velocity to be similar. Indeed, all sensors are located within the mean azimuthal velocity plateau ($r/R > 0.8$ in the LDV measurements).

2.2. Turbulence properties

We use the hot-wire as a reference probe to determine the turbulence properties in He I. It is a standard Pt–Rh hot-wire, driven using a DISA 55M10 constant temperature anemometer. The wire diameter is
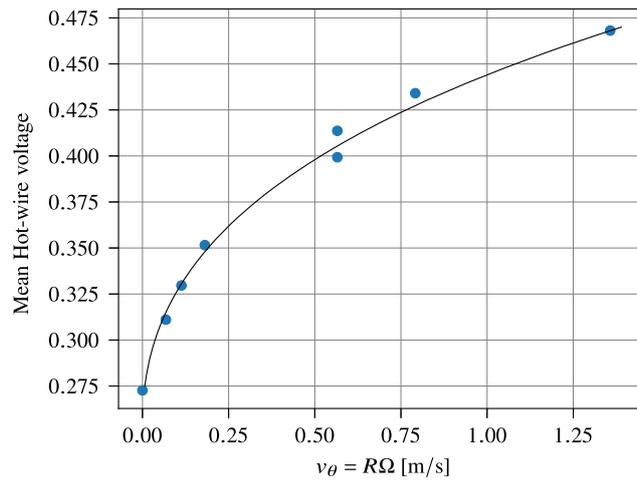
Figure 3. *In situ* calibration of the hot-wire anemometer in He I. Solid line: King's law fit equation (3).

Table 1. Summary of turbulence properties in He I.

f [mHz]	Ω [rad s^{-1}]	v_θ [m s^{-1}]	Re$_g$
30.0	0.19	0.07	1.1×10^6
50.0	0.31	0.11	1.9×10^6
80.0	0.50	0.18	3.0×10^6
250.0	1.57	0.57	9.5×10^6
350.0	2.20	0.79	1.3×10^7
600.0	3.77	1.36	2.3×10^7

1.3 μm. Its length is 300 μm. It is placed in the equatorial plane of the Von Kármán flow, about 4 cm from the wall. It is similar to the one discussed in [43], and previously tested in low temperature liquid helium-4.

As can be seen in figure 3, the hot-wire mean signal is compatible with the King law [44],

$$\mathcal{P} = a\sqrt{v_\theta} + b, \tag{3}$$

where $\mathcal{P} \sim E^2$ is an image of the heating power of the wire (E is the measured voltage), and $v_\theta = R\Omega$ is an estimate of the *co-rotation* azimuthal velocity, neglecting the $O(1)$ prefactor because it makes no difference at first order, and we do not know if the precise value of this prefactor has a Reynolds number dependency.

The main control parameter is the global Reynolds number, Re$_g$,

$$\text{Re}_g = \frac{R^2\Omega}{\nu}. \tag{4}$$

In He I, taking $\nu = 2.14 \times 10^{-8}$ m^2 s^{-1}, the global Reynolds number ranges from 1.1×10^6 for $\Omega = 0.19$ rad s^{-1} to 2.3×10^7 for $\Omega = 3.77$ rad s^{-1} (see table 1).

To determine the turbulence intensity, τ,

$$\tau = \frac{\sqrt{\langle v'^2 \rangle}}{v_\theta}, \tag{5}$$

an estimate of the variance of the velocity fluctuations, $\langle v'^2 \rangle$, must be computed from the velocity signals, where

$$\langle v'^2 \rangle = \left\langle \left(v(t) - \langle v \rangle \right)^2 \right\rangle. \tag{6}$$

The brackets, $\langle \cdot \rangle$, stand for temporal average.

For low velocities however, the signal-to-noise ratio of the hot-wire signal is quite small (≈ 0.6), so that computing the turbulence intensity using calibrated data would yield over-estimated values. Assuming the velocity data are affected by a constant (velocity independent) uncorrelated noise σ_{noise}, the apparent measured turbulence intensity, τ_{mes}, can be written

$$\tau_{\text{mes}} = \tau + \frac{\sigma_{\text{noise}}}{v_\theta}. \tag{7}$$
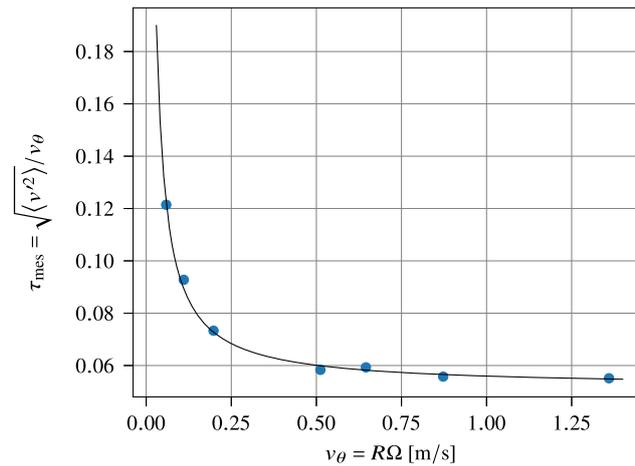
Figure 4. Measured turbulence intensity in He I, τ_{mes}, computed from the hot-wire velocity signal, as a function of the azimuthal velocity. Solid line: fit using equation (7).
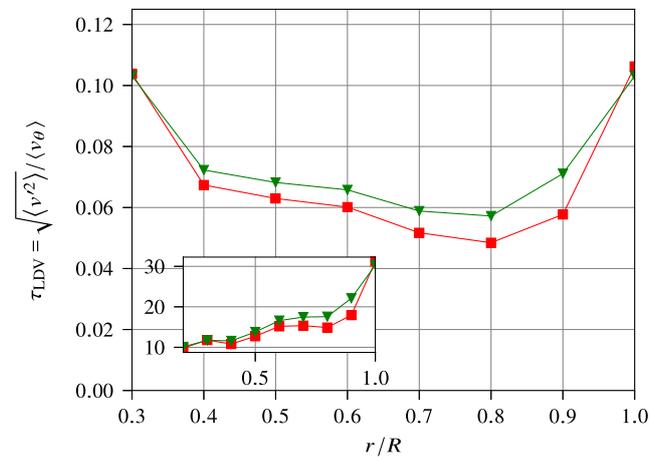

Figure 5. Profiles of turbulence intensity, obtained as the ratio of the standard deviation to the mean of the laser Doppler velocimetry measurements, at mid-height in the SPHYNX Von Kármán cell. Red squares: azimuthal velocity; green triangles: vertical velocity. The corresponding turbulence intensity close to the wall ($r/R > 0.8$) is between 5% and 10%, both for the azimuthal and the vertical components. Inset: velocity standard deviation in centimeters per second.

As shown in figure 4, fitting the experimental data with equation (7) leads to $\sigma_{noise} = 4.1$ mm s^{-1}, and $\tau = 5.2\%$. This level of turbulence intensity is consistent with the LDV measurements in the SPHYNX cell in water (see figure 5), and also to similar measurements obtained at even lower Reynolds number in air [45], suggesting that the turbulence intensity in this geometry does not depend much on the Reynolds number, over a large range of Re$_g$.

3. Velocity sensors in He II

3.1. Cantilever anemometer

The cantilever anemometer used in this work consists in a micro-machined silicon-oxide 260 μm $\times$ 35 μm $\times$ 1.2 μm beam, with a disk at its tip of diameter 100 μm (see the scanning electron microscope picture in figure 6). A strain gauge is deposited onto the beam. It is etched in a 1200 Å-thick sputtered nichrome layer. A sputtered 1400 Å-thick platinum meander is deposited onto the disk, but is not used in the present paper. Details about the fabrication, characterization, and validation of the sensor in wind tunnels and jets, both at room and low temperature can be found in [46]. In addition, the same type of sensor was used in liquid helium, and validated against a reference Pitot tube [14].

To increase the signal-to-noise ratio, we use dedicated electronic configurations, shown in figure 7, for the measurement of the mean signal and the measurement of its fluctuations. To measure the mean signal, the nichrome bridge is polarized with a carrier wave at frequency 7 Hz, and the bridge voltage imbalance is
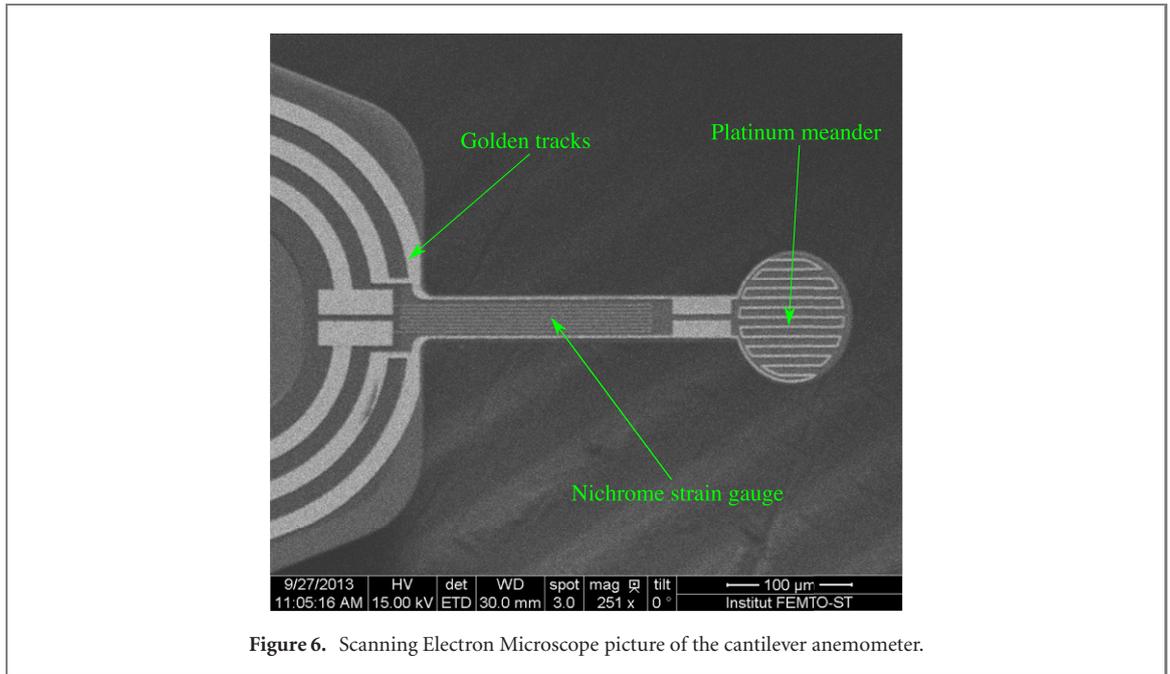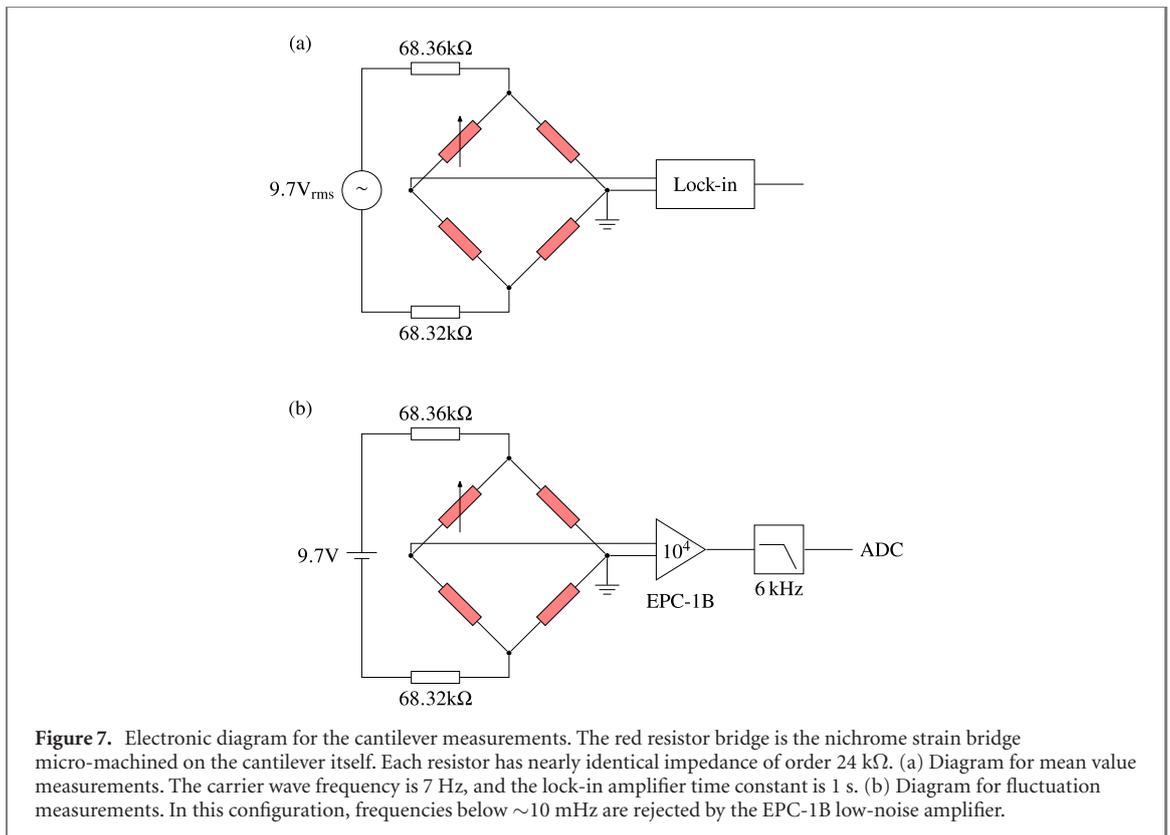
Figure 6. Scanning Electron Microscope picture of the cantilever anemometer.

Figure 7. Electronic diagram for the cantilever measurements. The red resistor bridge is the nichrome strain bridge micro-machined on the cantilever itself. Each resistor has nearly identical impedance of order 24 kΩ. (a) Diagram for mean value measurements. The carrier wave frequency is 7 Hz, and the lock-in amplifier time constant is 1 s. (b) Diagram for fluctuation measurements. In this configuration, frequencies below ~10 mHz are rejected by the EPC-1B low-noise amplifier.

demodulated with a lock-in amplifier. To measure the fluctuations, which are much smaller than the mean, the bridge is polarized with batteries, and we use the same low-noise high-gain amplifier which was used in [14] to amplify the bridge imbalance. This amplifier has a noise floor 0.7 nV/$\sqrt{\text{Hz}}$, and a low frequency cut-off of ~10 mHz.

The sensor Reynolds number, Re_{canti}, is defined with the disk diameter length scale, $\Phi_{\text{d}} = 100 \ \mu\text{m}$,

$$\text{Re}_{\text{canti}} = \frac{\Phi_{\text{d}} v_{\theta}}{\nu}. \tag{8}$$

It can be computed in He I where the kinematic viscosity is unambiguous, or in He II using $\nu = \mu/\rho$, which is a good estimate at large scales where both fluids are locked [11, 40], where μ is the dynamical
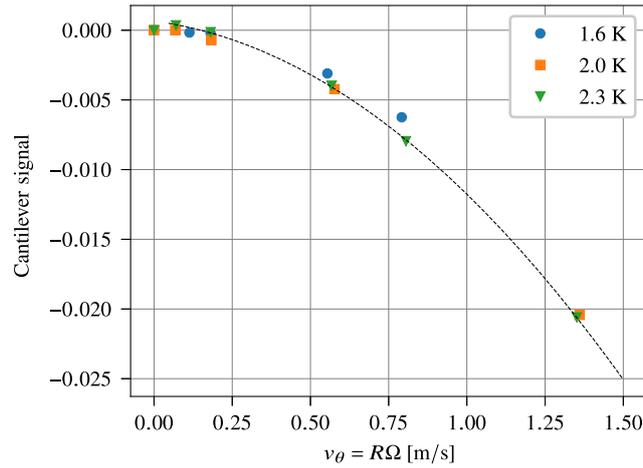
Figure 8. Mean cantilever signal for several mean azimuthal velocities and temperatures, both in He I (2.3 K), and in He II (1.6 K and 2.0 K). The dashed line is a quadratic fit.
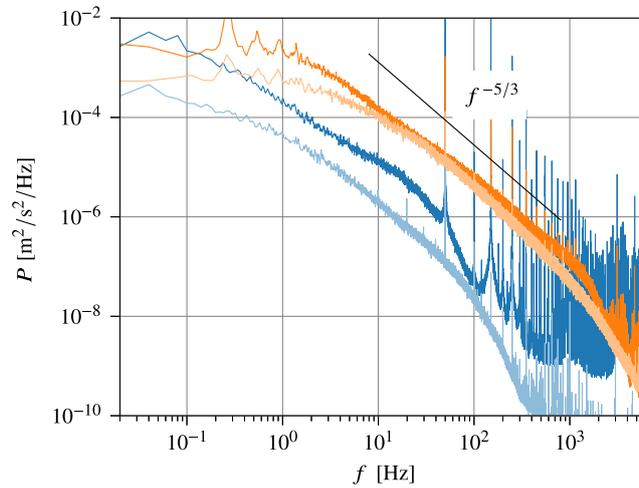

Figure 9. Turbulent velocity power spectra obtained with the cantilever in He I (2.3 K), using the quadratic calibration shown in figure 8 (dark lines), and the hot-wire (light lines) at angular velocities $\Omega = 0.50$ rad s^{-1} (bottom) and 3.77 rad s^{-1} (top). Black line shows the $-5/3$ slope.

viscosity of the normal component and ρ the total fluid density. There are other estimates for the effective viscosity of He II, such as those based on measurements of the vortex line density and the dissipation [17, 47–50]. Their order of magnitude is similar, so using them would not change the order of magnitude of the Reynolds number estimates. In the range of temperatures of the present paper, the value of ν in He II, 9.75×10^{-9} m^2 s^{-1} at 1.6 K, 1.14×10^{-8} m^2 s^{-1} at 2.0 K, is close to the value of ν in He I, 2.14×10^{-8} m^2 s^{-1} at 2.3 K. Therefore, there is no practical difference between He I and He II for the estimate of Reynolds numbers: they range between 330 and 6300 for the azimuthal velocities considered in this paper. At such Reynolds numbers, the drag force on the cantilever is expected to scale like ρv_θ^2, and to be identical above and below the superfluid transition [3–6]. As can be seen in figure 8, it seems indeed to be the case for the cantilever sensor in the present work, at least in a first approximation.

The velocity power spectra obtained from the hot-wire and the cantilever in He I can then be directly compared. As can be seen in figure 9, they differ, in particular the slope in the inertial range. However, the main features match, in particular the absolute value of the power density, the frequencies of the large scale plateau, the small scale cut-off, and the frequency of the forcing. In addition, neither of the probes produce spectra with an exact $-5/3$ slope. The reason for both the discrepancy between the probes, and the deviation from $-5/3$ slope, is that the flow is really neither isotropic nor homogeneous. However, for the sake of comparison between turbulence in He I and He II, this is not an issue.

The discrepancy appears to be larger at the lowest velocity, where the velocity fluctuations found by the cantilever appears to be larger. This is consistent with the velocity RMS profiles found in water (see

Figure 10. Schematic of the miniature Pitot sensor. (a) Side view. (b) Top view. The gap between the upper and lower parts is 20 μm.

Figure 11. Electronic diagram of the capacitive readout for the miniature Pitot sensor. (1) Top electrode; (2) membrane (mobile); (3) bottom electrode.
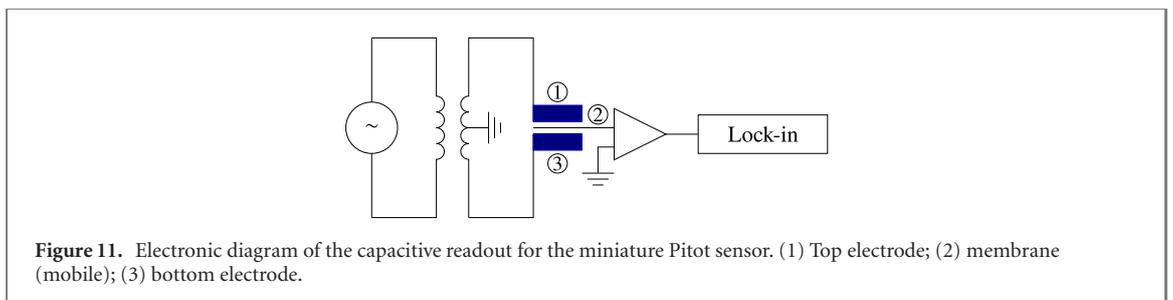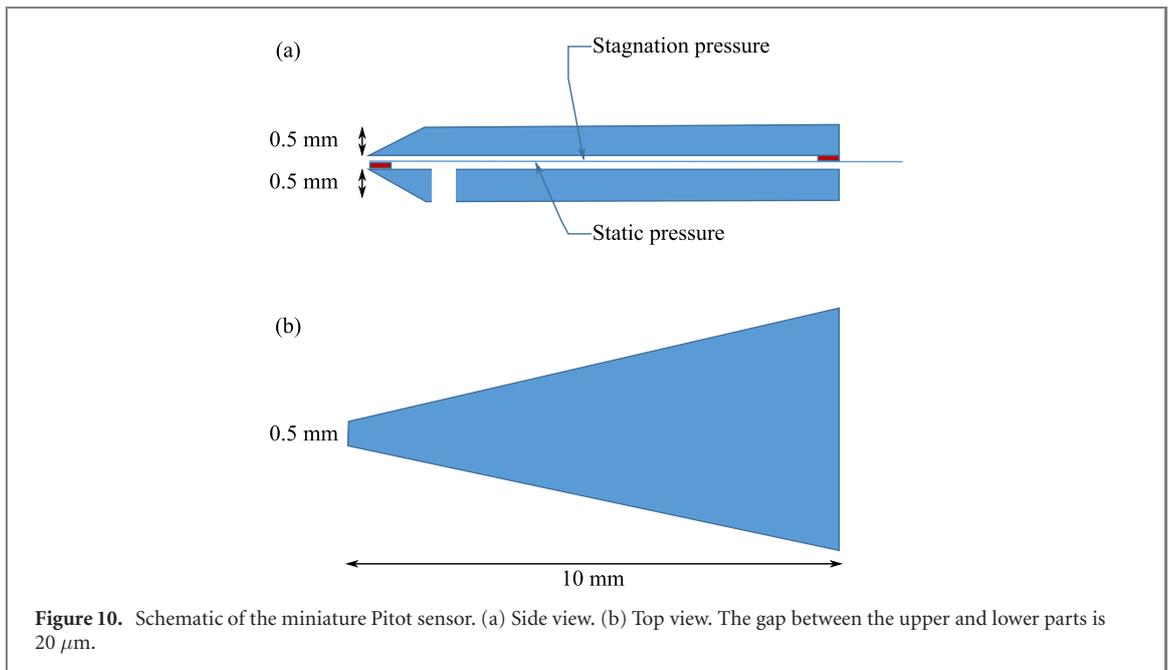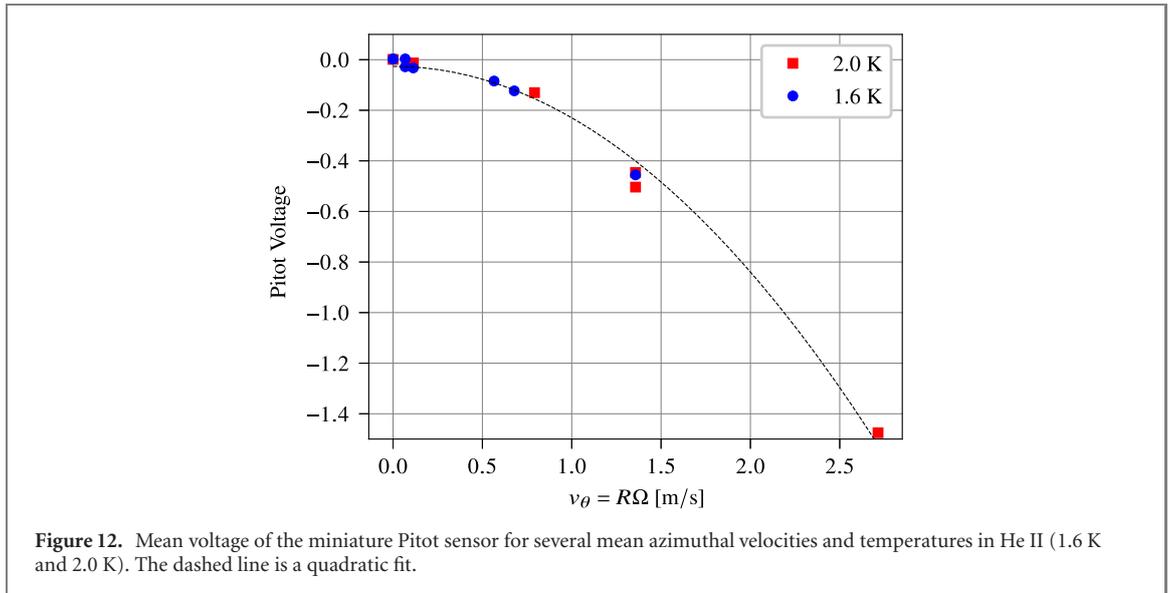
figure 5), which shows that the velocity RMS increases for $r/R > 0.9$. Yet we cannot also exclude that this discrepancy is a bias due to inaccuracy of the calibration at very low velocities. Indeed, the calibration procedure assumes that the azimuthal velocity is $r\Omega$, possibly with a constant prefactor. As can be seen in figure 2, we expect indeed that the mean velocity profile exhibits a plateau for $r/R > 0.8$. However, the cantilever anemometer is placed at $r/R = 0.97$. It is possible that the mean velocity profile, this close from the wall, would deviate from the plateau, and this deviation may depend on the angular velocity.

However, since the turbulence intensity is small, the cantilever response is actually expected to be very close to linear near the working point. Therefore, in the following, we will not attempt to use the quadratic calibration, but instead multiply the cantilever fluctuation signal by an ad-hoc prefactor, chosen for each operating condition to match the turbulence intensity measured by the hot-wire (5.2%) in He I (figure 4).

3.2. Miniature Pitot sensor
The miniature 'Pitot'-like sensor consists in a suspended diaphragm that allows to realize flow-velocity detection by measuring the pressure difference between stagnant fluid pressure in front of the sensor and static pressure in the flow around the sensor (figure 10), similarly to the sensors used by Berberig and collaborators [51]. In this work, we use a 25 μm brass membrane inside the sensor nose. At low temperature, the differential thermal contraction tends to stretch the membrane. The small gap (20 μm) and the flexibility of the membrane set the mechanical resonance of the system. The objective is to reduce mechanical resonance that limits the bandwidth of this type of sensor [13]. While the use of a larger gap and a stiffer membrane would increase the mechanical resonance frequency, they would also yield smaller sensitivity. The design choice for the present sensor is a compromise where sensitivity was chosen over frequency, to grant access to the lowest velocity flows where the dissipative range may be resolved. The membrane displacement is read using a dedicated capacitive bridge shown in figure 11.

Unlike the cantilever which ultimately measures the drag force, the Pitot tube does not require a breaking of the flow symmetry to become quadratic. Assuming the properties of the viscous boundary

Figure 12. Mean voltage of the miniature Pitot sensor for several mean azimuthal velocities and temperatures in He II (1.6 K and 2.0 K). The dashed line is a quadratic fit.

layers are identical in He I and He II, the miniature Pitot sensor measures the dynamical pressure,

$$s(t) = \frac{1}{2}\rho v(t)^2. \tag{9}$$

Therefore, it is not expected to deviate from the quadratic behavior at low velocity (see figure 12). This is an advantage because the calibration remains reliable over a wider range of velocities, and also a drawback because the sensitivity is lower in the low velocity limit (compared to sensor with linear, or square root sensitivity). Because the turbulence intensity is low, the fluctuation signal, $s'(t) = s(t) - \langle s \rangle$, can be linearized [13],

$$s'(t) = \rho \langle v \rangle v'(t) + \mathcal{O}(\tau^2). \tag{10}$$

Therefore, like the other sensors, the miniature Pitot response can be considered linear near each working point, and it is not a prerequisite to calibrate the signal to discuss the slope and the cut-off frequencies of the power spectra.

The miniature Pitot sensor is validated in He I against the hot-wire (see figure 13). Unlike the cantilever, they are at the same distance from the walls, and the statistical features are expected to match. It is indeed the case, both at low (0.31 rad s^{-1}) and high (2.20 rad s^{-1}) angular velocity. At low frequencies, the spectra are in good agreement. At high frequencies, the miniature Pitot signal deviates from the hot-wire signal either because of the noise floor (above 10 Hz for the low velocity signal), or because of the mechanical resonance (above 200 Hz for the higher velocity signal). The mechanical resonance peak frequency can be seen at $\approx$500 Hz on these spectra.
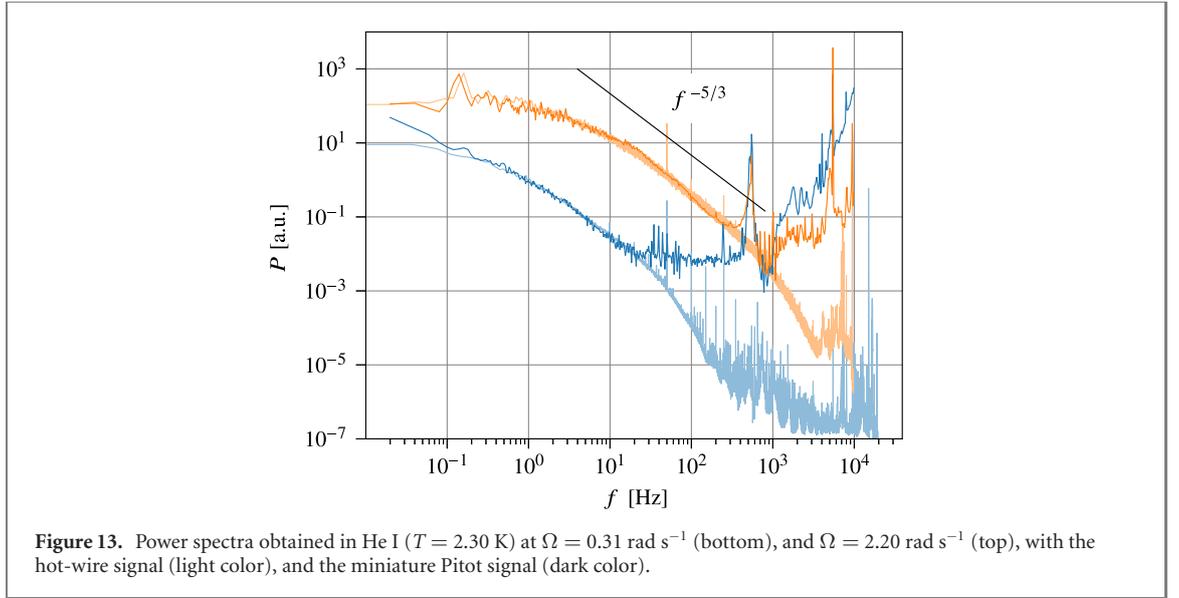
3.3. Discussion

The three sensors used in this work are complementary because they have different limitations: (i) the hot-wire is the reference sensor in He I but its use in He II would require comprehensive modeling that lies beyond the scope of the present paper; (ii) the sensitivities of the cantilever and the miniature Pitot sensors are well understood in both He I and He II, but their quadratic sensitivity makes them difficult to use in the zero-velocity limit. In addition, the Pitot sensor has a relatively low high-frequency limit caused by the mechanical resonance, which makes it unsuited to the high-velocity flows.

Both the cantilever and the miniature Pitot tubes are well documented kinds of sensors in cryogenic flows [13, 14, 46, 52], and the present ones have been further validated in He I against the hot-wire.

The best experimental compromise to investigate non classical signature of velocity spectra in He II consists in choosing a velocity low enough for the dissipative scales to lie within resolved frequencies, and high enough for the signal-to-noise ratio to be sufficiently large.

Below the superfluid transition, there are however two velocities, the velocity of the normal component, $\vec{v}_n$, and the velocity of the superfluid component, $\vec{v}_s$, and it is not trivial to know which velocity the sensors actually measure. In fact, both sensors are really sensitive to a local pressure load, typically the difference between dynamical and static pressures in the case of a Pitot tube, or the strain load on the beam in the case of the cantilever. The most simple assumption that has been usually made in the case of Pitot tubes [11, 12],

Figure 13. Power spectra obtained in He I ($T = 2.30$ K) at $\Omega = 0.31$ rad s^{-1} (bottom), and $\Omega = 2.20$ rad s^{-1} (top), with the hot-wire signal (light color), and the miniature Pitot signal (dark color).

and was extended to cantilevers [14], is that the measured signal $s(t)$ can be approximated as

$$s(t) = \frac{1}{2}\rho_n v_n^2 + \frac{1}{2}\rho_s v_s^2, \tag{11}$$

or equivalently,

$$s(t) = \frac{1}{2}\rho v_m^2 + \frac{\rho_n \rho_s}{2\rho}(v_n - v_s)^2, \tag{12}$$

where

$$v_m = \frac{\rho_n v_n}{\rho} + \frac{\rho_s v_s}{\rho} \tag{13}$$

is the barycentric velocity. When both fluids are locked, $v_n - v_s$ is small, so the sensors measure the barycentric velocity. Since we can only resolve the first few scales where the two fluids may start to unlock, we may assume that $v_n - v_s$ remains small, and the measured velocity is therefore close to the barycentric velocity.

4. Signature of quantum turbulence?
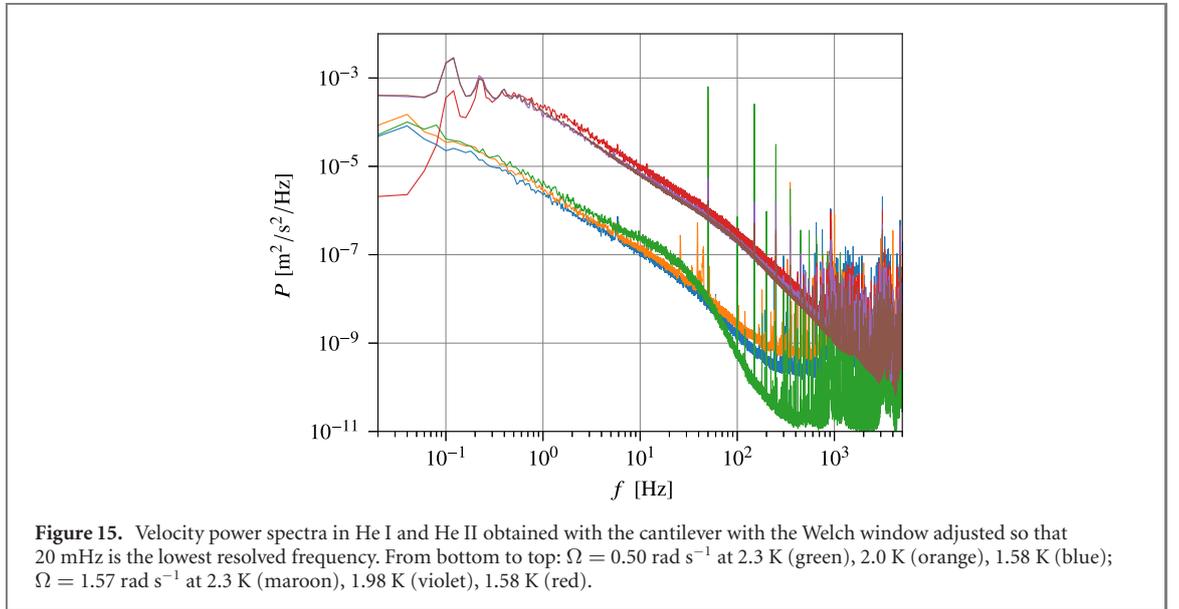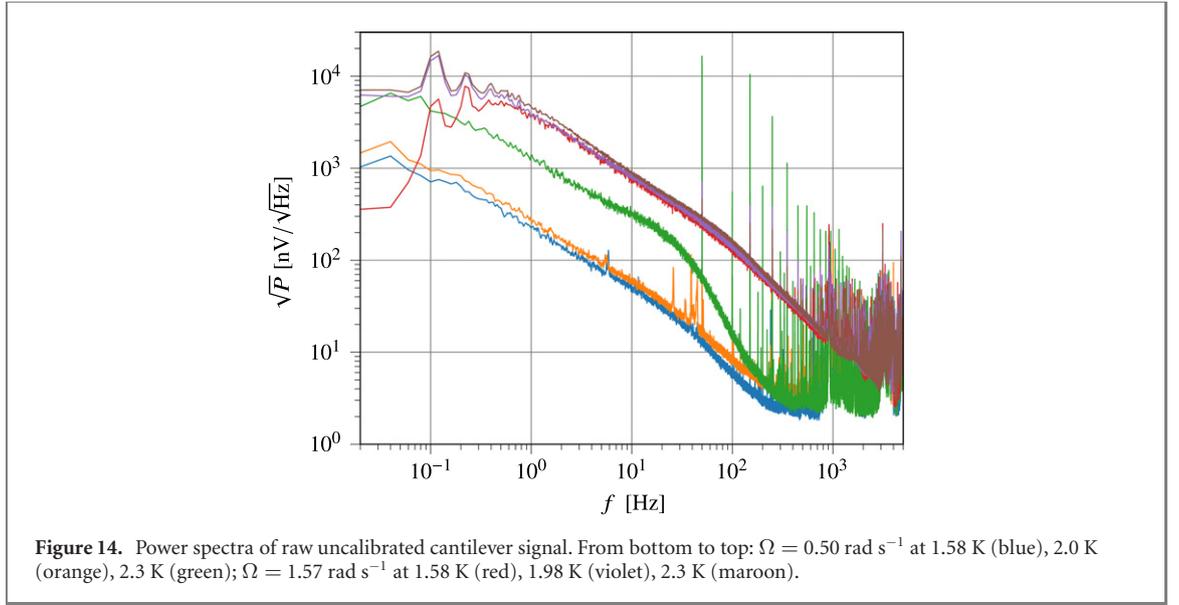
4.1. Velocity spectra in He I and He II
As can be seen in figure 14 and 15, at high velocities (1.57 rad s^{-1}), the velocity power spectrum is indistinguishable between He I and He II. This is consistent with many previous measurements in the turbulent regime where only the inertial scales are resolved [11–13]. At lower velocities (0.50 rad s^{-1}) however, one can see that the spectra differ at the smallest resolved scales.

More details can be seen in figure 16 where the spectra have been smoothed with a smaller Welch window. At large scales (or low frequencies), the measured velocity power spectra are identical, within the measurement uncertainties. However, for smaller scales, corresponding to frequencies higher than typically 100 Hz, the power density is higher in He II than in He I, and there may be a weak temperature dependence with higher energy level at 2 K than 1.58 K. The experimental data does not allow *a priori* to infer the value of cut-off scale in He II, nor can it distinguish between simply a higher cut-off frequency in He II, or a range of kinematic energy accumulation at meso-scales, as found in numerical simulations [53].

The same observation can be reported at a lower angular velocity (0.31 rad s^{-1}) where the miniature Pitot sensor shows the same kind of difference. The spectra shown in figure 17 evidence difference between He I and He II for frequencies of order of 10 Hz: at the smallest resolved scales, the power density in He II is higher than in He I.

4.2. Flow scales
As shown in table 1, the global Reynolds number of the flow ranges from 1.1×10^6 for $\Omega = 0.19$ rad s^{-1} to 2.3×10^7 for $\Omega = 3.77$ rad s^{-1}. However, the turbulence intensity in *co-rotation* is small, which this estimate for the Reynolds number does not take into account. A more meaningful definition of the Reynolds

Figure 14. Power spectra of raw uncalibrated cantilever signal. From bottom to top: $\Omega = 0.50$ rad s^{-1} at 1.58 K (blue), 2.0 K (orange), 2.3 K (green); $\Omega = 1.57$ rad s^{-1} at 1.58 K (red), 1.98 K (violet), 2.3 K (maroon).

Figure 15. Velocity power spectra in He I and He II obtained with the cantilever with the Welch window adjusted so that 20 mHz is the lowest resolved frequency. From bottom to top: $\Omega = 0.50$ rad s^{-1} at 2.3 K (green), 2.0 K (orange), 1.58 K (blue); $\Omega = 1.57$ rad s^{-1} at 2.3 K (maroon), 1.98 K (violet), 1.58 K (red).

number, is based on the mean fluctuating velocity $\sqrt{\langle v'^2 \rangle}$, and the longitudinal integral scale L_l, defined below

$$\mathrm{Re} = \frac{L_l \sqrt{\langle v'^2 \rangle}}{\nu}. \tag{14}$$

The longitudinal integral length scale, L_l is defined as,

$$L_l = \frac{1}{\langle v'^2 \rangle} \int_0^{+\infty} \langle v'(0) v'(r) \rangle \ \mathrm{d}r, \tag{15}$$

and can be deduced in He I, under the assumptions of homogeneous and isotropic turbulence, large Re, and Taylor's frozen turbulence, from the velocity power spectrum shown in figure 18, as done in reference [13]. Indeed, assuming an uncorrelated signal at low frequency, leading to a flat spectrum until frequency f_0, and then a Kolmogorov $-5/3$ power law, then

$$L_l \approx \frac{\langle v \rangle}{10 f_0} = \frac{1}{10 k_0}. \tag{16}$$

The large scale wave-vector, $k_0 = 3.5$ m^{-1} is found to be nearly the same in all hot-wire spectra. The corresponding longitudinal integral scale is 2.9 cm. The order of magnitude is comparable to the height of the blades (7.8 cm), which is consistent with previous such measurements [54] where the integral scale was found to be independent of the Reynolds number.
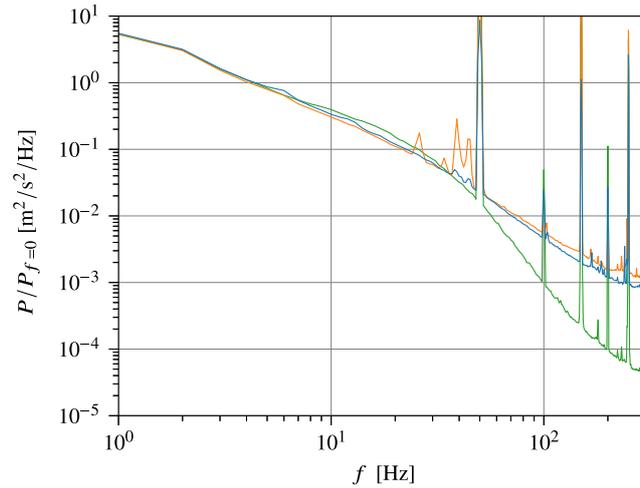
Figure 16. Cantilever-based velocity power spectra in He I and He II for $\Omega = 0.50$ rad s^{-1} with the Welch window adjusted so that 1 Hz is the lowest resolved frequency. The trend to saturation at high frequency is consistent with the expected noise floor from the electronics. Their level vary because of changes in sensor sensitivity. From bottom to top 2.3 K (green), 2.0 K (orange), 1.58 K (blue).
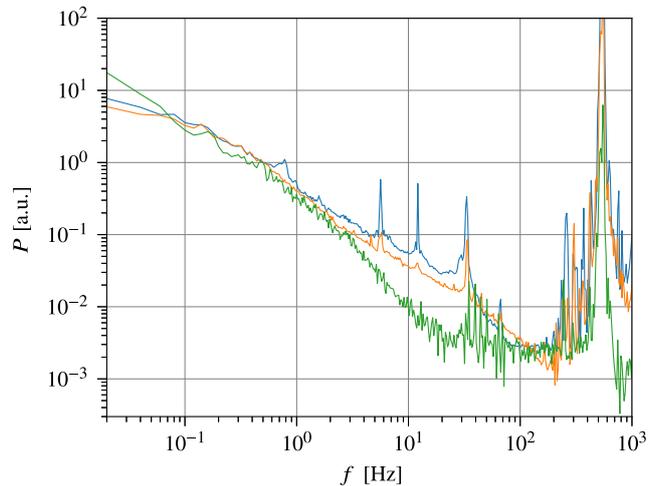

Figure 17. Velocity power spectra in He I and He II obtained with the miniature Pitot sensor for the angular velocity $\Omega = 0.31$ rad s^{-1}. From bottom to top: 2.3 K (green), 2.0 K (orange) and 1.58 K (blue).

From these estimates of the velocity fluctuation, and the integral scale, one can estimate the Reynolds number, and the Kolmogorov scale η, from the classical relationship,

$$\frac{\eta}{L_\mathrm{l}} = \mathrm{Re}^{-3/4}. \tag{17}$$

As can be seen in table 2, the Kolmogorov length scale is a fraction of the hot-wire length. However, the dissipative range starts at scales larger than the Kolmogorov scale [39]. For instance, Mydlarski and Warhaft [55] reported experimental turbulence spectra for a range of Reynolds numbers comparable to ours. From their compensated spectra (their figure 9), the viscous dissipative range spans below $\ell_\mathrm{DI} \simeq 100\eta$. At the lowest rotation rates, such a length scale is significantly larger than the hot-wire and cantilever dimensions: thus both anemometers have sufficient spatial resolution to probe the onset of the dissipative range.

In the experimental conditions of figures 15 and 16 ($\Omega = 0.50$ rad s^{-1}), the viscous dissipative range is thus expected to appear for frequencies beyond $f \simeq v_\theta/(100\eta) \simeq 75$ Hz, in reasonably good agreement with observations in He I (see green spectrum). Beyond this frequency, the scales resolved by the cantilever typically spans over $\log_{10}\left(100\eta/(2\Phi_\mathrm{d})\right) \simeq 1.1$ decade. In practice, the instrumental limitation does not arise from spatial resolution but from the background noise[10], as illustrated by figure 15. This is why the upper frequency of the plot in figure 16 is arbitrarily limited to 300 Hz, which corresponds to the length scale $v_\theta/f = 600$ μm.
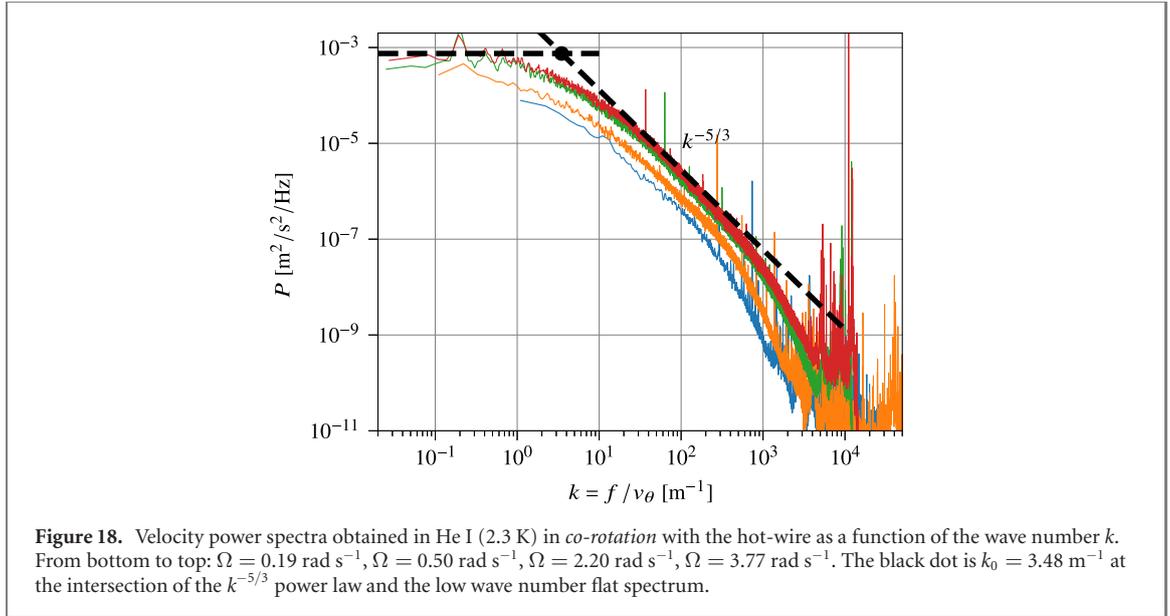
Figure 18. Velocity power spectra obtained in He I (2.3 K) in *co-rotation* with the hot-wire as a function of the wave number k. From bottom to top: $\Omega = 0.19$ rad s^{-1}, $\Omega = 0.50$ rad s^{-1}, $\Omega = 2.20$ rad s^{-1}, $\Omega = 3.77$ rad s^{-1}. The black dot is $k_0 = 3.48$ m^{-1} at the intersection of the $k^{-5/3}$ power law and the low wave number flat spectrum.

Table 2. Estimates of flow scales based on the fluctuating Reynolds number Re in He I.

Ω [rad s^{-1}]	v_{rms} [mm s^{-1}]	Re	η [μm]	λ [mm]	$\ell_{\mathrm{DI}} \approx 100\eta$ [mm]
0.19	3.5	4.8×10^3	50.5	1.3	5.0
0.31	5.9	8.0×10^3	34.4	1.0	3.4
0.50	9.4	1.3×10^4	24.2	0.8	2.4
1.57	29.4	4.0×10^4	10.3	0.5	1.0
2.20	41.2	5.6×10^4	8.0	0.4	0.8
3.77	70.6	9.6×10^4	5.3	0.3	0.5

4.3. Interpretation

The main result of the present work is the observation that turbulence spectra measured at low velocity in He I and He II overlap along a $\sim f^{-5/3}$ scaling at intermediate (inertial) scales—as expected from current understanding of quantum turbulence—but differ over a range of scales where viscous dissipation takes place in He I (see figure 16). At these dissipative scales, the spectra measured in He II fall between the He I spectrum and the continuation of the inertial range scaling, as if the He II was 'moderating' viscous dissipation, or as if some extra energy piles up at small scales.

   He II can be described as a mixture of a superfluid and a normal fluid, coupled by a mutual friction force. The relative mass fraction of superfluid is $\rho_{\mathrm{s}}/\rho = 83\%$ at 1.58 K, and 39% at 2.0 K and 3 bars. It has been shown in numerical simulations over a wide temperature range that the strength of mutual coupling is such that both fluid remain locked (or nearly so) at the large and intermediate scales of the turbulence cascade [56], but this locking cannot hold down to the smallest scales due to the inviscid nature of the superfluid [2, 41]. At scales where both fluids are locked, He II can be described as a single viscous fluid undergoing a classical turbulence cascade. Thus, the observation of differences between He I and He II spectra suggests that the superfluid and normal fluid are no longer locked at small scales. The one-decade disagreement between the unlocking scale measured by the cantilever (figure 16) and by the Pitot-like probe (figure 17) is not understood but one could speculate that the distance from the sidewall (resp. 1 cm versus 4 cm), or some blocking effect arising from the Pitot-like sensor design could contribute to the explanation. Neither probes have been characterized in flows when superfluid and normal velocities v_{s} and v_{n} are uncoupled. Still, the principle of operation based on the deflection of fluid momentum suggests that both probes are sensitive to the barycentric velocity of the flow v^*,

$$v^* = \frac{\rho_{\mathrm{n}}}{\rho} v_{\mathrm{n}} + \frac{\rho_{\mathrm{s}}}{\rho} v_{\mathrm{s}}, \tag{18}$$

at scales significantly larger than the probe dimension, which is the case at the dissipative scales of interest. Under this hypothesis, the enhanced spectra power density measured in He II would be explained by larger fluctuations in the normal and/or superfluid components. Incidentally, figure 16 shows a small excess of energy in He I around 20 Hz that we interpret as the standard 'bottleneck' preceding the viscous cut-off

(e.g. see [55, 57]). This bottleneck is expected to be more pronounced for steeper dissipative cut-out due to triadic interactions between wavenumbers [58, 59]. It is interesting to note that the bottleneck is smaller (if any) on the He II spectra, which is consistent with the milder cut-off at small scales.

A turbulent superfluid flow can be seen as an ordered tangle of quantum vortices. Such flow can be characterized by the quantum length scale δ, defined as the typical distance between vortices. In homogeneous isotropic turbulence, this scale can be estimated as [40, 53]

$$\delta = L_{\mathrm{l}}\left(\frac{\nu_{\mathrm{eff}}}{\kappa}\right)^{1/4}\left(\frac{v_{\mathrm{rms}}L_{\mathrm{l}}}{\kappa}\right)^{-3/4},\tag{19}$$

where $\kappa \simeq 10^7\ \mathrm{m^2\ s^{-1}}$ is the quantum of circulation around a single ^{4}He vortex, and ν_{eff} ranges from 0.1κ to 0.2κ in present temperature conditions [40]. In the experimental conditions in figure 16, one finds $\delta \simeq 50\ \mu\mathrm{m}$[11]. Thus, the length scales where He II differ from the He I spectra are tens of times larger than intervortex distance.

This observation is compatible with a prediction that a range of mesoscales appears in turbulent He II between the inertial scales, and the intervortex distance [53]. Over these mesoscales, the superfluid kinetic energy cascading from inertial scales has been predicted to pile up till the energy transfer to the normal fluid by mutual friction has become sufficiently efficient to dissipate energy. Consistently, direct numerical simulations of the two fluids at various temperatures found more energetic superfluid and normal velocity spectra. For instance, one may compare the experimental spectra in figure 16 to the *intermediate temperature* (1.96 K) and *low temperature* (1.44 K) velocity spectra obtained by numerical simulations (see figure 1 in reference [53]), in the short range of scales just beyond the start of the classical dissipative range. In this range of scales, it behaves as if the inertial range does continue, with the *intermediate temperature* spectrum slightly above the *low temperature* spectrum, consistently with present observations.

The spectra of figure 15 obtained at $\Omega = 1.57\ \mathrm{rad\ s^{-1}}$ do not evidence the same difference between the He I and He II flows. We have no interpretation for this observation, in apparent contradiction with the one at lower velocity. In particular, we cannot exclude that differences between spectra could be associated with different flow states. Further experiments are certainly needed to ascertain the present interpretation.

One may note that there is also a possible contribution of the thermal flow generated by the power dissipated in the bulk. In He I, the bulk get heated by turbulent dissipation, possibly producing buoyancy-driven flow. In He II, a steady counterflow may establish between the bulk and the top propeller where there is a heat exchanger. However, the total dissipated power is always below 10 W, which yields counterflow velocities less than $0.4\ \mathrm{mm\ s^{-1}}$, well below the turbulent counterflow threshold, and also below the sensitivity of our sensors. Similar argument can be made for the buoyancy-driven flow in He I, which is always much smaller than the mechanically produced flow.

5. Conclusion

Local velocity measurements have been performed in the SHREK *co-rotating* Von Kármán cell using a hot-wire, a miniature Pitot-like sensor, and a cantilever anemometer. At velocities large enough for developed turbulence to settle, but small enough for the dissipative scales to be experimentally accessible, differences between He I and He II velocity spectra are reported at the lowest accessible velocities (0.31 rad s^{-1} and 0.50 rad s^{-1}), but not at the higher one (1.57 rad s^{-1}). This condition in velocity is not yet understood. When some spectral differences are measured, we find more energy in He II than in He I in the resolved dissipative scales. The power density is slightly higher at 2 K than 1.58 K. The experimental observation is compatible with the prediction [53] that superfluid kinetic energy accumulates over a range of mesoscales at the bottom of the inertial cascade in turbulent He II. According to this interpretation, the observed increase of the spectral density is the signature of the absence of an efficient dissipative mechanism in the superfluid component compared to the normal fluid component of He II.

---

[11] The flow mean rotation at $\Omega = 0.50$ rad s^{-1} can be associated with a lattice of vortices of density $\delta^{-2} = 2\Omega/\kappa \simeq (316\ \mu\mathrm{m})^{-2}$ [60]. Since this distance is larger than the intervortex distance associated with turbulence, this rotational contribution to the effective intervortex distance is neglected.

Data availability statement

The data that support the findings of this study are openly available at the following URL/DOI: https://turbase.cineca.it/init/routes/#/logging/view_dataset/34/tabmeta

ORCID iDs

J Salort ⓘ https://orcid.org/0000-0003-3052-5898
F Chillà ⓘ https://orcid.org/0000-0001-7279-1057
E Rusaouën ⓘ https://orcid.org/0000-0002-9875-3187
P-E Roche ⓘ https://orcid.org/0000-0001-6175-4146
B Dubrulle ⓘ https://orcid.org/0000-0002-3644-723X
S Nazarenko ⓘ https://orcid.org/0000-0002-8614-4907

References

[1]   Tisza L 1947 *Phys. Rev.* **72** 838
[2]   Vinen W F and Niemela J J 2002 *J. Low Temp. Phys.* **128** 167–231
[3]   Smith M R, Hilton D K and Van Sciver S W 1999 *Phys. Fluids* **11** 751
[4]   Hemmati A M, Fuzier S, Bosque E and Van Sciver S W 2009 *J. Low Temp. Phys.* **156** 71–83
[5]   Blažková M, Schmoranzer D, Skrbek L and Vinen W F 2009 *Phys. Rev.* B **79** 054522
[6]   Ahlstrom S L *et al* 2014 *Phys. Rev.* B **89** 014515
[7]   Rousset B, Claudet G, Gauthier A, Seyfert P, Martinez A, Lebrun P, Marquet M and Van Weelderen R 1994 Pressure drop and transient heat transport in forced flow single phase helium II at high Reynolds numbers *15th Int. Cryogenic Engineering Conf.* vol 34 pp 317–20
[8]   Fuzier S, Baudouy B and Van Sciver S W 2001 *Cryogenics* **41** 453–8
[9]   Saint-Michel B *et al* 2014 *Phys. Fluids* **26** 125109
[10] Rusaouen E, Rousset B and Roche P-E 2017 *Europhys. Lett.* **118** 14005
[11] Salort J, Chabaud B, Lévêque E and Roche P-E 2012 *Europhys. Lett.* **97** 34006
[12] Maurer J and Tabeling P 1998 *Europhys. Lett.* **43** 29–34
[13] Salort J *et al* 2010 *Phys. Fluids* **22** 125102
[14] Rusaouën E, Chabaud B, Salort J and Roche P-E 2017 *Phys. Fluids* **29** 105108
[15] Holmes D S and Van Sciver S W 1992 *J. Low Temp. Phys.* **87** 73–93
[16] Skrbek L, Gordeev A and Soukup F 2003 *Phys. Rev.* E **67** 047302
[17] Niemela J J, Sreenivasan K R and Donnelly R J 2005 *J. Low Temp. Phys.* **138** 537
[18] Varga E, Babuin S and Skrbek L 2015 *Phys. Fluids* **27** 065101
[19] Bradley D I, Fisher S N, Guénault A M, Haley R P, O'Sullivan S, Pickett G R and Tsepelin V 2008 *Phys. Rev. Lett.* **101** 065302
[20] Roche P-E, Diribarne P, Didelot T, Français O, Rousseau L and Willaime H 2007 *Europhys. Lett.* **77** 66002
[21] Woillez E, Valentin J and Roche P E 2021 *Europhys. Lett.* (at press)
[22] Yamazaki T, Murakami M, Ichikawa N and Nakai H 1987 *Japan. J. Appl. Phys.* **26** 89
[23] Kubo W and Tsuji Y 2019 *J. Low Temp. Phys.* **196** 170–6
[24] Celik D and Van Sciver S W 2002 *Exp. Therm. Fluid Sci.* **26** 971–5
[25] Zhang T and Van Sciver S W 2005 *J. Low Temp. Phys.* **138** 865
[26] Bewley G P, Lathrop D P and Sreenivasan K R 2006 *Nature* **441** 588
[27] Paoletti M, Fisher M E, Sreenivasan K and Lathrop D 2008 *Phys. Rev. Lett.* **101** 154501
[28] Chagovets T V and Van Sciver S W 2015 *Phys. Fluids* **27** 045111
[29] Fonda E, Sreenivasan K R and Lathrop D P 2016 *Rev. Sci. Instrum.* **87** 025106
[30] Mantia M L 2017 *Phys. Fluids* **29** 065102
[31] Gao J, Marakov A, Guo W, Pawlowski B T, Van Sciver S W, Ihas G G, McKinsey D N and Vinen W F 2015 *Rev. Sci. Instrum.* **86** 093904
[32] Tang Y, Bao S, Kanai T and Guo W 2020 *Phys. Rev. Fluids* **5** 084602
[33] Jäger J, Schuderer B and Schoepe W 1995 *Phys. Rev. Lett.* **74** 566
[34] Bradley D I *et al* 2012 *Phys. Rev.* B **85** 224533

[35]　Zmeev D E *et al* 2013 *Phys. Rev. Lett.* **110** 175303

[36]　Walmsley P M and Golov A I 2017 *Phys. Rev. Lett.* **118** 134501

[37]　Gritsenko I A, Zadorozhko A A, Neoneta A S, Chagovets V K and Sheshin G A 2011 *Low Temp. Phys.* **37** 551

[38]　Varga E, Gao J, Guo W and Skrbek L 2018 *Phys. Rev. Fluids* **3** 094601

[39]　Pope S B 2000 *Turbulent Flows* (Cambridge: Cambridge University Press)

[40]　Babuin S, Varga E, Skrbek L, Lévêque E and Roche P-E 2014 *Europhys. Lett.* **106** 24006

[41]　Barenghi C F, L'vov V S and Roche P E 2014 *Proc. Natl Acad. Sci. USA* **111** 4647

[42]　Rousset B *et al* 2014 *Rev. Sci. Instrum.* **85** 103908

[43]　Durì D, Baudet C, Moro J-P, Roche P-E and Diribarne P 2015 *Rev. Sci. Instrum.* **86** 025007

[44]　King L V 1914 *Phil. Trans. R. Soc.* A **214** 373

[45]　Simand C 2002 Étude de la turbulence inhomogène au voisinage d'un tourbillon *PhD Thesis* École Normale Supérieure de Lyon

[46]　Salort J, Rusaouën É, Robert L, du Puits R, Loesch A, Pirotte O, Roche P-E, Castaing B and Chillà F 2018 *Rev. Sci. Instrum.* **89** 015005

[47]　Stalp S R, Niemela J J, Vinen W F and Donnelly R J 2002 *Phys. Fluids* **14** 1377

[48]　Chagovets T, Gordeev A and Skrbek L 2007 *Phys. Rev.* E **76** 027301

[49]　Vinen W F 2014 *J. Low Temp. Phys.* **175** 305–16

[50]　Zmeev D E, Walmsley P M, Golov A I, McClintock P V E, Fisher S N and Vinen W F 2015 *Phys. Rev. Lett.* **115** 155303

[51]　Berberig O, Nottmeyer K, Mizuno J, Kanai Y and Kobayashi T 1998 *Sensors Actuators* A **66** 93–8

[52]　Salort J, Monfardini A and Roche P-E 2012 *Rev. Sci. Instrum.* **83** 125002

[53]　Salort J, Roche P-E and Lévêque E 2011 *Europhys. Lett.* **94** 24001

[54]　Tabeling P, Zocchi G, Belin F, Maurer J and Willaime H 1996 *Phys. Rev.* E **53** 1613

[55]　Mydlarski L and Warhaft Z 1996 *J. Fluid Mech.* **320** 331–68

[56]　Roche P-E, Barenghi C F and Leveque E 2009 *Europhys. Lett.* **87** 54006

[57]　Donzis D A and Sreenivasan K R 2010 *J. Fluid Mech.* **657** 171–88

[58]　Frisch U, Kurien S, Pandit R, Pauls W, Ray S S, Wirth A and Zhu J Z 2008 *Phys. Rev. Lett.* **101** 144501

[59]　Agrawal R, Alexakis A, Brachet M E and Tuckerman L S 2020 *Phys. Rev. Fluids* **5** 024601

[60]　Donnelly R J 1991 *Quantized Vortices in Helium-II* (*Cambridge Studies in Low Temperature Physics*) (Cambridge: Cambridge University Press)

[61]　Virtanen P *et al* 2020 *Nat. Methods* **17** 261–72

[62]　Harris C R *et al* 2020 *Nature* **585** 357–62

[63]　Hunter J D 2007 *Comput. Sci. Eng.* **9** 90–5